metals

MDPI

Article

Liquid Copper and Iron Production from Chalcopyrite, in the Absence of Oxygen

Katrin E. Daehn, Caspar Stinn, Lucas Rush, Ethan Benderly-Kremen, Mary Elizabeth Wagner, Charles Boury, Brian Chmielowiec, Carolina Gutierrez and Antoine Allanore *

Massachusetts Institute of Technology, Department of Materials Science, Cambridge, MA 02142, USA
* Correspondence: allanore@mit.edu; Tel.: +1-617-452-2758

Abstract: Clean energy infrastructure depends on chalcopyrite: the mineral that contains 70% of the world's copper reserves, as well as a range of precious and critical metals. Smelting is the only commercially viable route to process chalcopyrite, where the oxygen-rich environment dictates the distribution of impurities and numerous upstream and downstream unit operations to manage noxious gases and by-products. However, unique opportunities to address urgent challenges faced by the copper industry arise by excluding oxygen and processing chalcopyrite in the native sulfide regime. Through electrochemical experiments and thermodynamic analysis, gaseous sulfur and electrochemical reduction in a molten sulfide electrolyte are shown to be effective levers to selectively extract the elements in chalcopyrite for the first time. We present a new process flow to supply the increasing demand for copper and byproduct metals using electricity and an inert anode, while decoupling metal production from fugitive gas emissions and oxidized by-products.

Keywords: copper; sulfur; iron; chalcopyrite; electrochemical reduction

check for updates

Citation: Daehn, K.E.; Stinn, C.; Rush, L.; Benderly-Kremen, E.; Wagner, M.E.; Boury, C.; Chmielowiec, B.; Gutierrez, C.; Allanore, A. Liquid Copper and Iron Production from Chalcopyrite, in the Absence of Oxygen. *Metals* **2022**, *12*, 1440. https://doi.org/10.3390/met12091440

Academic Editor: Hong Yong Sohn

Received: 19 July 2022
Accepted: 23 August 2022
Published: 29 August 2022

Publisher's Note: MDPI stays neutral with regard to jurisdictional claims in published maps and institutional affiliations.

Copyright: © 2022 by the authors. Licensee MDPI, Basel, Switzerland. This article is an open access article distributed under the terms and conditions of the Creative Commons Attribution (CC BY) license (https://creativecommons.org/licenses/by/4.0/).

1. Introduction

Copper was the first metal to be utilized by mankind and has been dubbed the 'metal of civilization.' Artifacts from Tal-i Iblis, Iran provide some of the earliest evidence of copper smelting in the fifth millennium BCE [1]. Since these early copper smelting crucibles, smelters and metallurgical practices have improved drastically, but the chemical principle behind copper extraction has remained the same. An exothermic roasting reaction uses oxygen to yield metallic copper from the sulfide ore. For chalcopyrite, $CuFeS_2$, the most abundant copper mineral, oxygen effectively separates the two main components of chalcopyrite from copper: iron is preferentially oxidized to iron oxide and collected in a molten silicate slag, while sulfur reacts to form sulfur dioxide (SO_2) [2]. Modern "Flash" smelters use oxygen-enriched air, to supply sufficient heat to autogenously maintain the operating temperature, while the concentrated SO_2 gas stream is collected and converted to sulfuric acid [3]. This technology has supported the recent era copper mining: the extraction of massive, relatively low-grade porphyry copper deposits. Coupled with flotation, low-grade ore is economically upgraded and processed at high-throughput, bolstering substantial growth in the global copper industry—in fact, production has quadrupled from 1970 to present [4]. Now, the supply of copper must roughly triple from present to 2050 to enable the transition to an electrified, low carbon society [5]. As the 'metal of civilization' is tasked with its most important role yet, a production process suited to current challenges must be pioneered.

Aggressive investment in copper mines and facilities is needed to close the looming copper supply gap [6]. However, a survey of undeveloped copper deposits found 96% present multiple forms of risk [7], originating from lower copper grades [8], more complex mineralogies, and more remote or ecologically sensitive locations. Existing open-pit operations are planning the costly transition to underground mining [9], while new mining

projects remain strongly protested by local communities [10]. The historic, devastating impacts of copper mining and smelting on neighboring communities and ecosystems are well-documented. More stringent environmental regulations have been adopted, but the essential features of smelting remain. Copper smelting dust (generated at a rate of 5–10% of the total input) and smelting slag (~2 t/t copper) must be managed as hazardous waste [11]. Conventional smelting is not suited to handle the increasing concentration of Group 15 elements (As, Sb, Bi) in ore deposits. These elements have high vapor pressures and exhibit erratic behavior during smelting, forming a variety of oxides and sulfides and partitioning between gaseous and condensed streams, all requiring monitoring and treatment [12]. Given the lack of solutions to these concurrent problems, investment in new copper projects is historically low and is currently insufficient to meet demand within this decade [13].

The supply of a host of elements beyond copper are threatened by the challenges above. Typical impurities in chalcopyrite include silver, gold, arsenic, bismuth, cobalt, nickel, rhenium, molybdenum, selenium and tellurium. The rejection of these elements during copper production is a crucial source for society. In fact, tellurium is supplied exclusively by copper production, while the majority of selenium and molybdenum is tied to copper [14]. These minor elements are recovered late in the production flow, as slimes during electrorefining, and can provide additional revenue to smelters [15]. However, Kavlak et al. [16,17] and Moats et al. [18] show that recovery efficiencies from mine to refined metal are extremely low: selenium and tellurium are in the range of 5%. Further, the production supply chain traverses the globe as copper concentrate, blister copper and copper cathodes are shipped for processing in separate continents. This leads to supply/demand inelasticity for the by-products [14], confounds proper compensation to the original miners for by-products [19], and prevents nations that own copper reserves from establishing a domestic supply of copper and critical materials. As demand for these minor metals skyrockets and the transition to a clean energy economy hinges on their availability [20], such drastic inefficiencies must be addressed.

Processing pathways alternative to smelting for chalcopyrite (see Figure 1) have been sought for over a century. While alternative routes are commercially practiced for copper oxides and secondary copper sulfides (Cu_2S), distinct processing challenges arise due to the presence of iron, which is in equimolar proportion with copper in chalcopyrite. The refractory nature of chalcopyrite necessitates harsh processing conditions for hydrometallurgical techniques: high pressure, strong oxidants, or both. Recently, leachant additives such as iodide show some promise to act as a catalyst [21]. However, Habashi [22] documents a long-line of commercial hydrometallurgical ventures that have failed. In addition to oxidative leaching, process window exists to reduce metallic copper while iron remains in acidic solutions, but the co-evolution of hydrogen at the cathode is a key hindrance [23]. Carbo-thermic reduction was demonstrated, e.g., by Habashi and Yostos [24], but the solid pellets recovered contained long copper filaments in a black mass of iron particles, requiring subsequent leaching with hydrochloric acid. For higher productivity, carbothermic reduction may also be performed in the molten phase [25], but direct CO_2 emissions are high.

In the last main process pathway, electrons may be used as the reducing agent via electrolysis. Direct electrolytic processes powered solely by renewable energy offer a pathway to fully decouple metal production from greenhouse gas emissions. Over the last decades of the 20th century, copper smelters have incorporated more electrical power into their operations. Electrical energy may provide upwards of 85% of the smelting energy requirement in modern facilities [26], but the maximum reduction in global warming potential for this strategy is limited, around 60% [27]. The direct electrolysis of molten sulfides has been considered since 1906 [28], but was not very efficient due to the semi-conducting nature of sulfides at moderate and high temperatures. Chloride salts at intermediate temperatures have been investigated as an electrolyte, but both copper and iron exhibit multi-valency and co-deposit as a solid [29,30]. Halide as well as borate [31] electrolytes have limited solubility for the sulfide feedstock. A molten sulfide-based electrolyte would allow high feedstock

solubility, supporting high productivity. Recently, Sokhanvaran et al. [32] showed that with a sufficiently ionically conducting supporting electrolyte (BaS in this case), faradaic reactions may be supported to decompose Cu_2S to collect liquid metallic copper and gaseous sulfur using an inert graphite anode. Managing iron alongside copper in chalcopyrite remains however a key challenge [33].

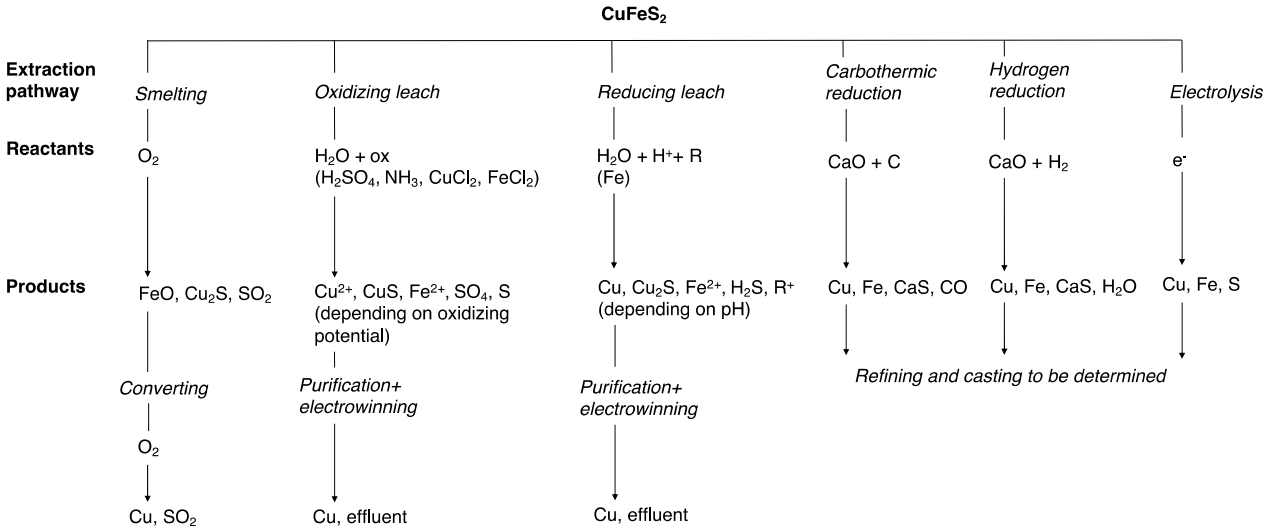

Figure 1. Investigated pathways to extract copper from chalcopyrite. Ox: oxidant, R: reductant.

Here, we present experimental results for the electrolytic decomposition of chalcopyrite to liquid iron and copper and gaseous sulfur by molten sulfide electrolysis. By excluding oxygen and processing chalcopyrite as a sulfide, unique opportunities arise in the supply chain from ore to final product that may address the challenges facing the copper industry. More broadly, the search for an inert, readily-available anode has thwarted the electrification and full decarbonization of commodity metals production. When minerals are processed as sulfides, the graphite anode is found to be inert, offering a process space crucial for sustainable metals production.

2. Materials and Methods

To investigate the electrochemical deposition of iron and copper, electrochemical experiments were performed at two scales: 300 mA (0.2 g electrolyte and cathodic surface area of 0.2 cm^2) and 7A (~60 g electrolyte and cathodic surface area of 8.0 cm^2), described in Sections 2.1 and 2.2, respectively. An equilibration experiment between cast iron and the electrolyte was performed to understand the relative activities between iron and copper in the system, as described in Section 2.3.

2.1. Electrochemical Experiments at the 300 mA Scale

Chalcopyrite concentrate was used in the 300 mA experiments. The characterization of the initial concentrate is described in Section 2.1.1. To prepare the chalcopyrite prior to electrolyte synthesis (described in Section 2.1.4), it was sulfidized (see Section 2.1.2) and gangue oxide phases were removed (see Section 2.1.3). In addition to the chalcopyrite-containing electrolyte, a series of electrolyte samples were synthesized with an increasing proportion of Cu_2S in relation to FeS to explore the deposition of copper and iron, described in Section 2.1.5. The equipment and procedure for performing galvanostatic electrolysis at the 300 mA scale with a graphite cathode and anode is described in Section 2.1.6. The post-experiment observation methods are described in Section 2.1.7. Thermal-only trials were performed in the absence of electrolysis to determine the extent of mass loss due to thermal decomposition at the electrolysis temperature, as described in Section 2.1.8. Lastly, a series of experiments were performed on copper and cast iron cathodes within a graphite stand at the 300 mA scale, with the set-up described in Section 2.1.9.

2.1.1. Chalcopyrite Concentrate: Characterization

Chalcopyrite concentrate after milling and flotation was graciously provided by Freeport McMoRan (Phoenix, AZ, USA) as a 25 kg bucket. To ensure accurate sampling of the elements and phases present for the initial characterization, representative portions were taken using the 'cone and quarter' sampling technique, repeated until samples weighing ~3 g were obtained. Samples were sent for inductively-coupled plasma mass spectrometry (ICP-MS) and LECO analysis, as well as lost-on-ignition analysis, performed by Massachusetts Materials Research Inc. (West Boylston, MA, USA). The composition measured by ICP-MS and LECO are shown in Table 1, while the lost-on-ignition analysis revealed a moisture content of 5.8 wt%. X-Ray Diffraction (XRD) quantitative crystalline phase analysis was also performed by H&M Analytical Services (Cream Ridge, NJ, USA), with the results shown in Table 2 and the phase identification scan shown in Figure S1.

Table 1. Elemental composition of the initial chalcopyrite concentrate feed from FreePort McMoRan, average of two samples measured by ICP-MS and LECO.

Element	wt%
Copper	25.8
Iron	31.65
Sulfur	28.85
Silicon	3.1
Zinc	0.24
Aluminum	0.645
Lead	<0.01
Arsenic	<0.01
Gold	<0.01
Silver	0.12
Molybdenum	0.18
Calcium	0.395
Sodium	0.215
Carbon	0.145
Hydrogen	0.385
Oxygen	5.5

Table 2. Quantitative crystalline phase analysis by XRD of the initial chalcopyrite concentrate.

Phase	wt%
$CuFeS_2$ (chalcopyrite)	49.0
FeS_2 (pyrite)	11.8
$Cu(SO_4)(H_2O)_5$ (chalcanthite)	26.3
$Cu_4(SO_4)(OH)_6$ (brochantite)	5.3
SiO_2 (quartz)	5.6
Unknown phases	~2

2.1.2. Sulfidation

To remove moisture, the concentrate was heated in a rotovapor. The quartz bulb containing 250 g concentrate with 350 mL ethanol was suspended in a mineral oil bath heated by a hotplate. The concentrate and ethanol mixture was held for several hours at ~100 °C at moderate-high rotation speed. Heating continued until the smoking point of the mineral oil (~220 °C) and vacuum was applied for several additional hours. The concentrate dispersed through the apparatus and could not be fully recovered. Total mass loss was 17 g.

To further remove residual moisture and oxygen, the concentrate was heated in a sulfur-rich atmosphere in a 'sulfidation' process. This methodology can be found in full in Stinn and Allanore (2021) [34] with the relevant details for chalcopyrite sulfidation described here. A total of 230.6 g of the dried concentrate was loaded into a graphite

crucible (25.4 mm OD, 9.5 mm ID, 25.4 mm depth, graphitestore, Northbrook, IL, USA) machined with approximately 20 evenly spaced, small (5 mm OD) holes machined in the bottom, which allowed sulfur gas flow through the chalcopyrite powder, while avoiding significant loss of the chalcopyrite powder from the bottom. The graphite crucible was positioned in the hot zone of a vertical tube furnace (PS400-120-20CLT-C2778-R-OT Mellen, Concord, NH, USA) using an alumina support tube. A stainless steel 316 crucible (13 mm OD, 12 mm ID, depth 75 mm, bottom thickness 5 mm) was loaded with approximately 250 g elemental sulfur powder (99.5%, sublimed, Acros Organics, NJ, USA). The powder was consolidated by carefully melting with a heat gun and cooled using an ice bath to ensure solidification without voids. The crucible was loaded into the bottom of the furnace, inside the alumina support tube and raised by a stainless steel rod (6 mm OD) introduced in the bottom port. The furnace chamber consisted of an alumina tube (600 mm length, 25 mm OD, 21 mm ID, Advalue Technology, Tucson, AZ, USA). A 1" diameter quartz tube was used for the outgas line and connected to a gravity separator constructed in-house to capture solidified sulfur particles. Argon (ultra-high purity Airgas, Radnor Township, PA, USA) was purged through the system at 600 sccm for approximately 30 min prior to heating. During the experiment, 600 sccm flowed through the chamber. The furnace was heated to 900 °C at 4.25 °C/min, held for 2 h and cooled at 5 °C/min. Once the 900 °C peak temperature was reached, the sulfur-containing crucible was raised from the bottom of the furnace at a rate of 0.5 cm per minute to provide sulfur gas flow through the furnace at a partial pressure of 0.05–0.2 atm. The total mass of the concentrate after sulfidation was 243.6 g. The sample was immediately transferred to a glove box for storage and a sample was sent to H&M Analytical for XRD analysis. The results of quantitative crystalline phase analysis can be seen in Table 3 and the phase identification scan shown in Figure S2.

Table 3. Quantitative crystalline phase analysis by XRD of the chalcopyrite concentrate after sulfidation.

Phase	wt%
$CuFeS_2$ (chalcopyrite)	87.9
FeS_2 (pyrite)	4.8
$(Cu_{10}Fe_2)S_4$ (nukundamite)	3.2
FeO(OH) (Lepidocrocite)	2.5
SiO_2 (quartz)	1.6

2.1.3. Oxide Phase Removal

After sulfidation, the concentrate contained residual oxide (gangue) phase, SiO_2, as shown in Table 3. Sulfides and most of the other oxides phase separate upon melting, so the sulfidized concentrate was heated in an inert atmosphere in the same furnace described above, but outfitted with 6.3 mm OD stainless steel tubing for the gas outlet. A graphite crucible was loaded with 223.7 g of the sulfidized concentrate. The tube furnace was evacuated by vacuum (−30 psig) and purged with argon three times. The furnace was heated to 1050 °C (just above the melting point of the sulfide phase) at 4.25 °C/min and held for two hours, then cooled at the same rate. Significant vaporization of excess sulfur from the previous step was observed and the total sample weighed 186.2 g afterwards. As can be seen in Figure S3, the sample did not melt completely (the inner portion remained solid because the temperature at the center of the furnace was not high enough). However, the outer ring that melted and re-solidified was the sulfide phase. A piece of this melted portion was separated and transferred to the glove box for electrolyte synthesis.

This procedure was improved to demonstrate the full separation of the oxide and sulfide phases. An induction heating system (UPT-Ultra Heat M Induction Heating System, 25 kW, Ultraflex Power, Ronkonkoma, NY, USA) with a sealed 76 mm diameter quartz tube was used to melt the concentrate. A total of 148.11 g of concentrate was loaded into a graphite crucible (25.4 mm OD, 9.5 mm ID, 25.4 mm depth, graphitestore) and positioned in the hot zone by a supporting fire brick and alumina rod. The power was increased until the concentrate was visibly molten (about 40% power) and held for 10 min, then

quenched. The glassy black silicate slag atop the sulfide matte can be seen in Figure S4. The slag was easily removed. The final masses were 9.46 g for the slag, and 111.96 g for the matte, matching well the weight percent of the silica and unidentified phases in the initial concentrate (Table 2). ICP analysis of this matte revealed the oxygen content had been reduced to 0.12 wt%.

2.1.4. Electrolyte Synthesis: Chalcopyrite

In previous work, Stinn et al. [35] demonstrated the high solubility of copper sulfide (Cu_2S) in barium sulfide (BaS). A mixture of BaS and lanthanum sulfide (La_2S_3) was used as the supporting electrolyte in this investigation (binary system characterized by Boury and Allanore [36]). Sokhanvaran et al. [32] show that this supporting electrolyte supports ionic transport, while the decomposition voltage of BaS and La_2S_3 are sufficiently high. Chalcopyrite concentrations in excess of 20 wt% are miscible within the BaS-La_2S_3 system. To mitigate electronic conductivity, chalcopyrite was dissolved at 10 wt%. However, the relationship between electronic conductivity and current efficiency is not established from a firm physical and chemical basis [37], and there may be avenues to increase this proportion with greater insight into the electrolyte properties and mechanisms involved in electrochemical deposition.

The sulfidized and oxide-separated chalcopyrite concentrate from above was ground with a mortar and pestle in the glove box. The target composition of the electrolyte was 55.8 wt% BaS (99.7% metals basis, Alfa Aesar, Ward Hill, MA, USA), 34.2 wt% La_2S_3 (99.0% metals basis, Alfa Aesar), and 10 wt% sulfidized chalcopyrite, $CuFeS_2$. The powdered contents were mixed by shaking in a vial. The electrolyte powder was divided to ~200 mg portions and loaded into a graphite circular puck (50 mm OD, graphitestore) machined with ~6 mm OD holes. The electrolyte droplets were pre-melted in the Mellen furnace, with a similar procedure and temperature profile as above, but to a peak temperature of 1350 °C for three hours. This pre-melting step also served to expel sulfur gas via thermal decomposition prior to electrolysis. Gaseous sulfur evolves such that $CuFeS_2$ transforms to ~$CuFeS_{1.8}$ [38]. The resulting electrolyte droplets of ~200 mg had a volume of about 65 mm^3.

To verify that carbothermic reduction did not occur during synthesis (possible if residual oxygen is present with graphite), the synthesized electrolyte was characterized by optical microscopy and scanning electron microscopy (SEM) using the procedure described below. No metallic phase was found. A typical SEM image of the electrolyte is shown in Figure S5, with the results of the EDS scan of the electrolyte shown in Figure S6 and Table S1. The synthesized droplets were also sent for ICP-MS analysis by Massachusetts Materials Research to confirm the elemental composition. The results are provided in Table 4 below.

Table 4. The ID, molar fraction of copper and iron (in sulfide form) and molar ratio of copper to iron, as well as the composition (wt%) as measured by ICP-MS and LECO for each initial electrolyte for the 300 mA experiments.

ID	Natural Chalcopyrite	Slight Cu_2S Enrichment	Moderate Cu_2S Enrichment	High Cu_2S Enrichment	Maximum Cu_2S Enrichment
Molar fraction Cu, Fe	0.5 Cu, 0.5 Fe	0.65 Cu, 0.35 Fe	0.75 Cu, 0.25 Fe	0.85 Cu, 0.15 Fe	0.95 Cu, 0.05 Fe
Molar ratio Cu:Fe	1:1	1.86:1	3:1	5.67:1	19:1
			Composition (wt%)		
Fe	3.6	2.4	1.6	0.9	0.24
Cu	3.7	5	6.2	6.9	7.6
S	21.4	21.8	20.2	20.8	20
La	31.4	30.3	28.1	32	30.6
Ba	44.7	46	46.9	41.8	42.4

2.1.5. Electrolyte Synthesis: Cu_2S Enrichment

Experimental results described in Section 3 show that iron deposits preferentially to copper from the chalcopyrite-containing electrolyte. To study the electrolysis product as FeS is depleted from the electrolyte, the initial electrolyte compositions were enriched with Cu_2S. A total of 200 mg electrolyte droplets were synthesized with the same procedure described in 2.1.4, but the chalcopyrite portion was substituted with Cu_2S and FeS powders. In all cases, the supporting electrolyte (BaS and La_2S_3) constituted 90 wt%, while the electro-active species (Cu_2S and FeS) constituted 10 wt%. Cu_2S (99.5% metals basis, Alfa Aesar) and FeS (99.9% metals basis, Alfa Aesar) powders were mixed to vary the molar ratio of copper and iron in the initial electrolyte, for increasing enrichment of copper sulfide. The identifying label (ID) of each electrolyte, the molar ratio and fraction of copper to iron (both in sulfide form) and their composition in wt% as measured by ICP-MS and LECO can be seen in Table 4.

2.1.6. Electrolytic Reduction on Graphite Cathode at the 300 mA Scale

A thermal imaging furnace (TIF, TX-12000-I-MIT-VPO-PC, Crystal Systems Corp., Yamanashi, Japan) equipped with four Xe lamps (12 kW total) and ellipsoidal mirrors was used to heat the synthesized electrolyte droplets. The furnace was modified to support electrochemical measurements, as first described by Nakanishi and Allanore [39]. Graphite was used for the cathode and anode materials in this set of experiments. Graphite has been demonstrated to be stable and inert in the presence of molten sulfides during electrolysis above 1200 °C [32] and no measurable mass loss of the anode was observed over the course of these experiments. The electrolyte was supported on a graphite stand cathode, machined from a graphite rod (fine extruded, 6.3 mm OD, 305 mm L, graphitestore) to 14 mm length with a divet (4.9 mm OD, 2.25 mm deep) in the top to hold the droplet and provide a cathodic surface area of approximately 0.2 cm^2. On the other end of the stand, a hole was drilled and threaded to secure to a molybdenum rod (>99.97%, 3.2 mm OD, 600 mm length, Ed Fagan, Franklin Lakes, NJ, USA). The molybdenum rod was sheathed in an alumina tube (>99.8%, 6.35 mm OD, 4 mm ID, Coorstek, Golden, CO, USA) and introduced through the bottom port as the electrode probe. The graphite anode was machined from the same graphite rod to a total length of 18 mm, with a 2 mm OD tip, 5 mm long, tapered to a sharp point. The opposite end was also drilled and threaded to secure a molybdenum rod sheathed in an alumina tube. Both the anode and cathode graphite pieces were sonicated in acetone and dried prior to use. The anode electrode probe was introduced from the top port. Ultratorr fittings were used to seal the top and bottom ports. The assembly of probes and sample were protected from the ambient atmosphere in a quartz tube (custom, Technical Glass Products Inc., Painesville, OH, USA) sealed with Viton O-rings. A camera (EOS Rebel T5i DSLR, Canon Inc., Tokyo, Japan) was used to monitor and video record the sample assembly in the hot zone. The vertical position of the probes were controlled by stepper motors with sub-millimeter precision.

A Gamry Reference 3000 potentiostat was used for galvanostatic electrolysis. The cell potential was recorded using an Omega data acquisition system (OMB-DAQ-54). The sealed quartz tube was evacuated by vacuum and filled three times with ultra-high purity argon (Airgas). After purging, the argon gas flow rate was set to 300 sccm. Across all experiments, the apparatus was not equipped with an oxygen sensor, but previous experimental work with this equipment and procedure measured pO_2 ~10^{-5} atm under these conditions [39]. The Xe lamps were powered on and the electrolyte sample was heated for 3 min at 3% power while rotating the bottom probe at 5 rpm to form a stable molten droplet. Rotation of the bottom probe was then stopped, and the anode was inserted from the top. An image of the molten droplet on the graphite cathode with the graphite anode inserted can be seen in Figure S7. Galvanostatic electrolysis of 300 mA was applied for 30 s for a high cathodic current density of ~1.5 A/cm^2. Two electrolysis experiments were performed for each electrolyte composition in Table 4. Experimental notes from each trial can be seen in

Table S2. Voltage traces for these experiments can be seen in Figures S8–S16. After 30 s, the lamps were shut off to quench the sample, with cooling rates greater than 100 C/s.

2.1.7. Post-Experiment Observation

The mass change (Δm) of the electrolyte, anode and cathode were measured following electrolysis. Several of the droplets broke into multiple pieces during handling after electrolysis. In these cases, the mass loss is greater than expected and was not used for further analysis. When the droplet remained intact, Faradaic efficiency estimates were calculated from the mass loss of the electrolyte, assuming sulfur gas (S_2) as the evolved anodic product with a four-electron transfer process. The theoretical mass loss was calculated with Faraday's law (Equation (1)), where m: theoretical mass loss, Q: Coulombs passed, F: Faraday's constant (96,485.33 C/mol), M: molar mass, and z: valency.

$$m = \frac{QM}{Fz} \quad (1)$$

Thermal trials (described below in Section 2.1.8), where the same heating procedure was performed in the absence of electrolysis, were used to determine the sulfur evolved from thermal decomposition, and this quantity was subtracted from the total measured after electrolysis.

Samples were cast in epoxy (Allied High Tech Products Inc., Rancho Dominguez, CA, USA) and cured in air for 24 h, then ground using silicon carbide sandpaper and mineral oil as a lubricant, followed by polishing with a non-aqueous diamond suspension (Allied High Tech Products Inc.). Observations were made using an optical microscope (Olympus BX51, Olympus, Tokyo, Japan) and scanning electron microscopes (JEOL JSM-6610LV, JEOL Ltd., Tokyo, Japan). The SEM was equipped with energy dispersive spectroscopy (EDS, Sirius SD detector, SGX Sensortech Ltd., Corcelles-Cormondreche, Switzerland) for elemental analysis.

2.1.8. Thermal-Only Trials in the Thermal Imaging Furnace

To determine mass loss due to thermal decomposition in the absence of electrolysis, thermal trials were performed. The heating procedure was identical to the electrolysis experiments: 3% power for 4 min 30 s. The anode was inserted similarly, but no current was applied. The mass loss was found to be 2.16 mg.

The electrolyte cross-section was characterized to determine if metal production occurred in the absence of electrolysis, shown in Figure S17. A few droplets of metallic iron (all of which are depicted) were found at the interface with graphite due to oxygen contamination and carbothermic reduction. This minor oxygen contamination was present despite the gas control procedures and storing the electrolyte in the glovebox. However, the observed metal production was significantly less than the droplets observed in the electrolyzed samples, as shown in Figures 3, 5, S27 and S30.

Further, a trial was performed in a more extreme heating profile and with vacuum applied to investigate whether metal production would result from decomposition. The natural chalcopyrite-containing electrolyte was heated on a graphite stand at 10% lamp power for a total of six minutes with 5 rpm rotation. For the final three minutes −10 psig vacuum was applied. The cross section of the electrolyte afterwards is shown in Figure S18. The mass loss was slightly higher at 3.32 mg, but minimal metal production was found.

2.1.9. Electrolytic Reduction and Thermal Trials on Copper and Cast Iron Cathodes at the 300 mA Scale

To investigate electrolytic deposition on cast iron and copper cathodes, the graphite stand described in Section 2.1.6 was modified. The graphite stand was machined to have a deeper divet (3.5 mm) in the top to hold the electrolyte and metal. In profile, the stand was machined to have an hourglass shape (6.2 mm diameter tapering to 3.5 mm diameter, over the length of the divet) and four small holes (2 mm diameter) were drilled in the sides to

expose the cast iron or copper to the thermal heat from the xenon lamps. The same cast iron originally synthesized for the 7A iron deposition (Section 2.2.2) was used, but as shavings from turning the larger puck on the lathe. About 8 mg of cast iron shavings were added beneath the electrolyte droplet act as the cast iron cathode. One small ball of copper shot (Alfa Aesar, 1–10 mm, 99.9% purity, metals basis) weighing 10–15 mg was used for each copper cathode.

The same procedure as described in Section 2.1.6 was used for electrolytic reduction, with experimental notes provided in Table S3 and voltage traces shown in Figures S19–S24. Note that for the trial with the maximum enriched electrolyte to the copper cathode, there were unstable voltage readings for the first 15 s. The anode was further lowered such that the readings stabilized at 2.5–2.25 V, ran for an additional 15 s.

Thermal-only trials in the absence of electrolysis were also performed with varying initial electrolyte compositions on liquid cast iron and copper cathodes. The same procedure as the one described in Section 2.1.8 was used, but with the modified graphite stand as described above.

The post-experiment characterization was similar to that described in Section 2.1.7. For the cast iron cathode trials, the mass loss was not reliable because small cast iron shavings would fall from the stand during set-up, so they are not included. The mass loss from the maximum-Cu thermal was also not included due to the slightly different heating profile.

2.2. Electrolysis at the 7A Scale

To investigate electrolytic reduction at a larger scale, one experiment was performed at 7A with a cast iron cathode.

2.2.1. Electrolyte Synthesis

The electrolyte was the same composition as described in Section 2.1.4, but chalcopyrite was substituted with Cu_2S (99.5% metals basis, Alfa Aesar) and FeS (99.9% metals basis, Alfa Aesar) powders mixed such that copper and iron were in equimolar proportion. The mixture was premelted in a graphite crucible the Mellen furnace under argon. Upon cooling, the electrolyte was crushed and stored in the glovebox. A sample was sent for ICP-MS and LECO analysis. The composition is shown in Table S6.

2.2.2. Cell Preparation

The cell consisted of an alumina crucible (>99.8%, 25.4 mm OD, 22.5 mm ID, 99.6 mm depth, 101.6 mm height, Coorstek) with a 6.3 mm hole drilled in the bottom. An alumina tube (>99.8%, 6.3 mm OD, 4.8 mm ID, 57.9 mm length, Coorstek) was inserted into another alumina tube (>99.8%, 9.53 mm OD, 6.35 mm ID, 34.3 mm length, Coorstek) such that 6.4 mm of the internal tube was exposed at the bottom end. Alumina paste (Resbond 940HT, Cotronics, Brooklyn, NY, USA) was used to seal together these two concentric tubes and to seal these tubes into the hole in the bottom of the alumina crucible. A brick of magnesia-chrome (MgO-Cr_2O_3) was machined with a tile saw and masonry drill bit to enclose the alumina crucible to act as secondary containment, while still fitting within the 63 mm ID furnace tube. The magnesia-chrome secondary containment was attached to the alumina crucible with alumina paste. All alumina had been cleaned in 1 M nitric acid at 200 °C for 3 h and washed in deionized water, then baked at 1000 °C in air for 10 h prior to assembly.

To provide the electrical connection to the liquid cast iron cathode, an iron rod (99.8%, 6.35 mm OD, 101.6 mm length) was inserted into the concentric alumina tubes to touch the bottom of the alumina crucible. The opposite end of the iron rod was drilled and threaded to secure a molybdenum rod (>99.97%, 3.17 mm OD, 300 mm length, Ed Fagan). The molybdenum rod was sheathed in an alumina tube (>99.8%, 6.35 mm OD, 1.6 mm ID, 200 mm length, Coorstek). Quick-set high temperature epoxy was used to seal the alumina tube to the end of the molybdenum. Ultratorr fittings sealed the anode and cathode leads

to the tube furnace. The schematic of the cell in the alumina furnace tube can be seen in Figure S25.

To synthesize the cast iron cathode, 45.0 g of graphite and 350.0 g electrolytic iron (high-purity, Tophet Corporation, Naples, FL, USA) were loaded in an alumina crucible (99.8%, 55.4 mm OD, 48.9 mm ID, 122.9 mm depth, 125.7 mm height). The alumina crucible was cleaned in nitric acid as described above. The iron and graphite were heated in the Mellen tube furnace (after vacuum purging three times and with argon flowing) to 1450 °C at 3 °C/min heating rate and held for six hours. The composition of the cast iron measured by ICP and LECO is shown in Table S4.

For the anode, a graphite puck (38.1 mm OD, 40 mm depth, graphitestore) was machined to a point with an inclined (~30°) plane. The graphite anode was cleaned in acetone in a sonicator. The top of the anode was drilled and threaded to be secured to a molybdenum rod (>99.97%, 3.17 mmOD, 300 mm length, Ed Fagan), which was sheathed in an alumina tube (>99.8%, 6.35 mm OD, 1.6 mm ID, 200 mm length, Coorstek). Quick-set high temperature epoxy was used to seal the alumina tube to the molybdenum rod at the cold end.

2.2.3. Electrolytic Reduction at the 7A Scale

The cell, containing 65.6 g electrolyte and 34.4 g of cast iron cathode, and electrode probes were loaded into the Mellen tube furnace. The chamber was vacuum purged three times, and the argon flow rate was set to 600 sccm. The furnace was heated to 1400 °C at 3 °C/min. Once the internal temperature peaked at about 1300 °C for 20 min, the anode was lowered until electrical contact with the electrolyte was achieved. Galvanostatic electrolysis was applied using a KEPCO power supply (KEPCO, BOP 20–20 M). The voltage was measured at the anode lead, cathode lead and either side of a shunt with a known resistance of 2.08 mΩ. Current was calculated by measuring the voltage drop across the known resistance of the shunt with Ohm's Law. Voltage was measured with high-frequency data acquisition loggers (DT9837B, DataTranslation, Norton, MA, USA) at 2.5 kHz. The cathode area was 8.02 cm^2 and the current density was set for 1 A/cm^2. The measured cell voltage was approximately 4 V for the duration of the run. In total, 5,952.4C was passed during the experiment. The voltage trace can be seen in Figure S26. Throughout the experiment, the concentration of SO_2, CO, CO_2 and H_2S in the outlet flow was measured with an infrared sensor (Infrared Industries, IR-208, Hayward, CA, USA). After running for approximately 13 min, the furnace was quenched.

2.2.4. Post-Experiment Observation

Once cool, the electrolyte and cathode were broken apart from the alumina crucible. A dispersion of the metallic product was found in the electrolyte at the interface with the cathode. The electrolyte was finely crushed using an agate mortar and pestle, and a neodymium magnet was used to separate any iron products from the crushed powder. This process was repeated over three cycles of milling and magnetic separation. A sample of the cathode was sent for analysis by ICP-MS and LECO.

2.3. Thermodynamic Analysis of Cu/Fe Deposition: Equilibration

An equilibration experiment was performed between the electrolyte utilized in the 7A experiment above and cast iron to determine the distribution of the electroactive species. The cast iron was synthesized from small pieces of graphite rods (fine extruded, 6.3 mm OD, graphite store) and high-purity electrolytic iron (Fe, Tophet Corporation) under an argon atmosphere in the presence of a zirconium oxygen getter (Zr, Alfa Aesar, 99.5% metals basis excluding Hf, Hf 3%). LECO analysis found the cast iron contained 5 wt% C.

The supporting electrolyte from the 7A experiment was ground into powder in the glove box and added to an alumina crucible with the cast iron. A piece of alumina was placed atop the crucible as a loose-fitting cap to minimize volatilization, and the entire setup was loaded into a vertical tube furnace (Lindberg/Blue MTM Mini-MiteTM, Riverside, MI,

USA). The crucible was supported by an alumina stage containing an alumina-sheathed "Type R" thermocouple. After applying the vacuum and purging three times, the sulfide and cast iron were heated to 1300 °C in an argon atmosphere and held for 24 h, followed by quenching by lowering the sample out of the hot zone and increasing the argon flow rate.

Upon cooling, the cathode was separated from the electrolyte. The composition of the cathode was measured with SEM-EDS, as described in Section 2.1.7.

3. Results

The findings from the electrochemical decomposition of chalcopyrite at the 300 mA scale is described in Section 3.1. These findings were further confirmed with a larger experiment at the 7A scale, also described in Section 3.1. Thermodynamic analysis was used to interpret these observations and investigate the selective deposition of iron and copper in Section 3.2. In Section 3.3, the electrolyte was enriched in Cu_2S to investigate the deposition of copper on the graphite, copper and cast iron cathodes.

3.1. Electrochemical Decomposition of Chalcopyrite

The main reaction describing the electrochemical decomposition of chalcopyrite to produce liquid copper is below, conducted between 1200 and 1450 °C.

$$(CuFeS_{1.8}) \rightarrow Cu(l) + Fe(s\ or\ l) + 0.9S_2\ (g) \quad (2)$$

Chalcopyrite thermally decomposes above 1000 °C in an inert atmosphere to evolve gaseous sulfur and transform to sulfur-poor β-chalcopyrite ($CuFeS_{2-x}$), which may accommodate a sulfur-deficiency of up to 15 wt%. The further decomposition to bornite, Cu_5FeS_4 and pyrrhotite, $Fe_{1-x}S$, has been proposed, though bornite most likely evolves during cooling and is not present in the molten state [38]. Here, we represent the β-chalcopyrite as $CuFeS_{1.8}$ for simplicity. The key challenge of chalcopyrite electrowinning is managing iron and copper separation in a selective manner. FeS and Cu_2S have similar standard state decomposition potentials, with only 54 mV difference at 1300°C, shown in Figure 2. The co-deposition of iron and copper at the cathode would therefore be expected upon the electrolytic decomposition of $CuFeS_2$. However, galvanostatic electrolysis experiments reveal that iron deposition is favored.

The metal product at the cathode interface following electrolysis of the chalcopyrite-containing electrolyte at the 300 mA scale (described in Section 2.1.6) is shown in Figure 3. Metallic iron was the only cathodic product observed. The composition of this phase contained less than 5 wt% copper, measured by SEM-EDS. Several additional micrographs showing the metallic iron product can be seen in Figure S27.

Galvanostatic electrolysis at larger scale (7A, 20 times the production rate at the 300 mA scale, described in Section 2.2) confirm these findings. The set-up was enhanced to include a liquid cast iron cathode to improve recovery of the metal product (schematic in Figure S25), and the gas outflow was equipped with an infrared sensor for analysis of the gaseous products. While the anodic product, gaseous sulfur, could not be directly detected with the sensor, the signals for CO(g) and H_2S(g) increased during electrolysis (Figure S28), suggesting the presence of anodic faradaic reactions. Dissolved oxygen and hydrogen anions present at low concentrations in the initial electrolyte are likely discharged at the anode. The oxygen anion then reacts with the carbon anode to form CO(g), while any trace of hydrogen reacts with the sulfur present. The delay in time between the increase in CO(g) and H_2S(g) and the application of current is due to the time it takes for the outlet gas to travel to the infrared sensor. Sulfur deposits (confirmed with SEM-EDS, Figure S29) were found on the furnace cap and dispersed throughout the gas line.

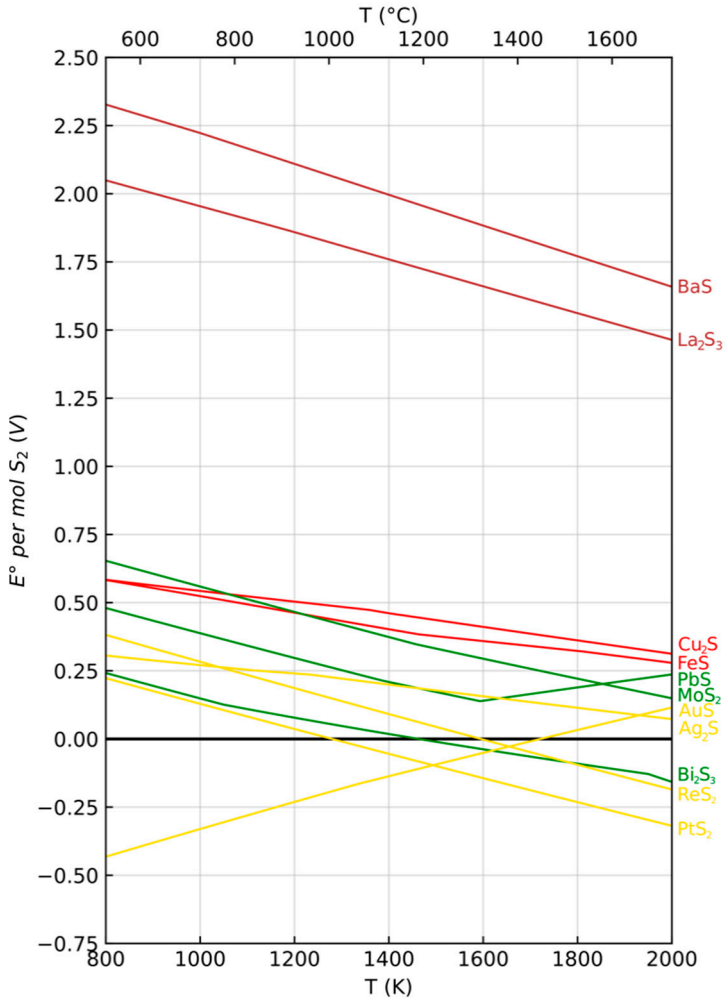

Figure 2. Sulfide Ellingham diagram with standard state decomposition voltage.

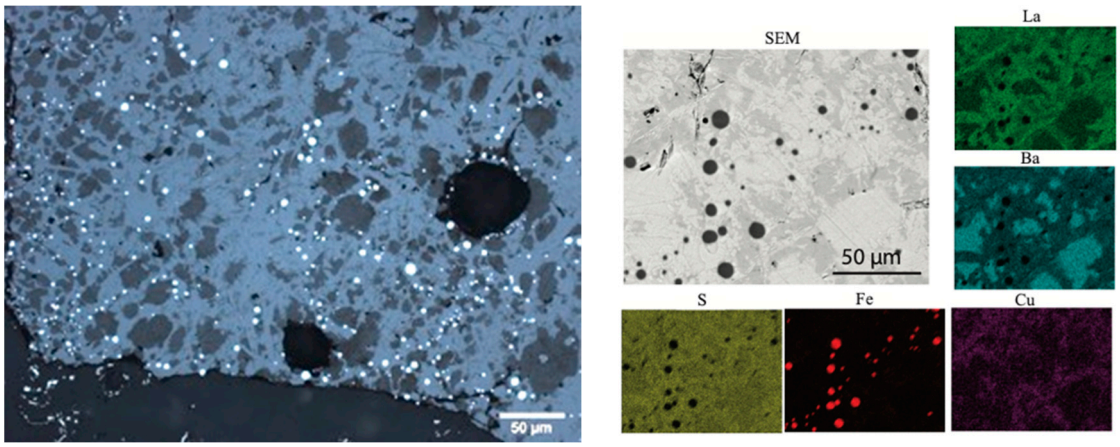

Figure 3. Iron-rich metallic product found on the graphite cathode after the electrochemical decomposition of $CuFeS_2$ concentrate in BaS-La_2S_3 supporting electrolyte, at 300 mA scale show in optical image (**left**) and SEM-EDS mapping (**right**). EDS analysis confirmed the cathodic product is iron-rich (>95%) with <5 wt% copper.

Following electrolysis, recovery of the cell contents revealed a metallic cloud present above the cathode. Dispersion of the metal product is the result of solidifidation and surface tension effects at this scale – as observed in the early development of the Hall-Heroult

electrolysis for aluminum, solidification studies of Cu-Fe melts [40] and other small batch experiments [41,42]. The electrolyte was crushed with a mortar and pestle and the metal product was recovered via magnetic separation. The increase in metallic iron was about 1.1 g (Table S5), consistent with approximately 64% faradaic efficiency, where two electrons are transferred per atom of Fe. The copper content of the cast iron cathode following electrolysis was 0.64 wt% (Table S6), which may be attributed to the thermodynamic drive for copper mixing in the cast iron cathode.

3.2. Thermodynamic Analysis of Selective Deposition

Thermodynamic analysis provides insight into the selective deposition of iron and copper. There is a high energy of mixing for copper and iron atoms in a liquid metal solution. Figure 4a shows the Cu-Fe-C phase diagram with a large gap of miscibility, further enhanced by the presence of carbon in the iron phase (i.e., cast iron). The equilibrium electrochemical synthesis diagram [43] for the Cu-Fe-C system (Figure 4b) accounts for these interactions, and discloses the possibility for selective iron and copper deposition. In this system, the product at equilibrium is predicted to be iron-rich with up to ~2.3 wt% Cu (X_{Cu} = 0.02). This system was modeled using FactSage 7.3, with the FTmisc, FScopp and FStel databases.

To investigate the non-standard behavior of Cu_2S and FeS in the novel BaS-La_2S_3 molten sulfide electrolyte, the thermodynamic framework described by Wagner and Allanore [44] was used. The Wagner-Allanore reference state describes the relative activities of two electroactive species in a multi-component supporting electrolyte, as demonstrated for the Cu_2S-Ag_2S system [44]. The relative coefficient, ρ_B, can be expressed as a ratio between two Raoultian activity coefficients, γ_B and γ_A, such that:

$$\rho_B = \frac{\gamma_B}{\gamma_A} \tag{3}$$

This is useful as direct measurement or calculation of the activities of the electroactive species in this system is not currently possible due to the lack of stable thermodynamic or electrochemical reference necessary to perform a traditional activity study. To determine the relative activities for copper and iron in the BaS-La_2S_3 electrolyte, the chemical equilibrium between the electrolyte with 10 wt% $CuFeS_2$ and cast iron was experimentally studied. It was found that ρ_{Cu2S} was 0.46, indicating Cu_2S has a lower activity relative to FeS in the electrolyte. Using this value generates a new electrochemical synthesis diagram (Figure 4c), suggesting preferential deposition of iron. The supporting electrolyte solvates Cu_2S differently to FeS, leading to the relatively higher stability of Cu_2S as a sulfide. This is a remarkable departure from the solid-state mixing thermodynamics of chalcopyrite where Cu_2S and FeS are often considereed to mix as in an ideal solution. Our findings that alkaline and alkaline earth sulfides can manipulate this mixing behavior are consistent with prior work [45], for the application of FeS-BaS fluxes to remove copper from carbon-saturated iron melts without electrolysis. In those conditions too, alkaline metal sulfides were found to effectively decrease γ_{Cu2S}, making alkaline sulfides good candidates for iron and copper separation.

3.3. Copper Deposition

Our results and analysis reveal an unexpected processing space for the electrochemical separation of iron and copper from chalcopyrite. During the extraction of iron from the chalcopyrite concentrate, Cu_2S will enrich in the electrolyte as more iron is produced and recovered at the cathode. The effect of this Cu_2S enrichment on the cathodic product was further investigated in a series of experiments performed on a graphite cathode. Cu_2S and FeS were mixed in varying proportion to yield initial electrolyte compositions with slight, moderate, high and maximum Cu_2S enrichment (compositions provided in Table 4 and Figure 5). Galvanostatic electrolysis was performed as described in Section 2.1.6. The compiled micrographs revealing the deposited metal product over the range of initial electrolyte composition are shown in Figure 5.

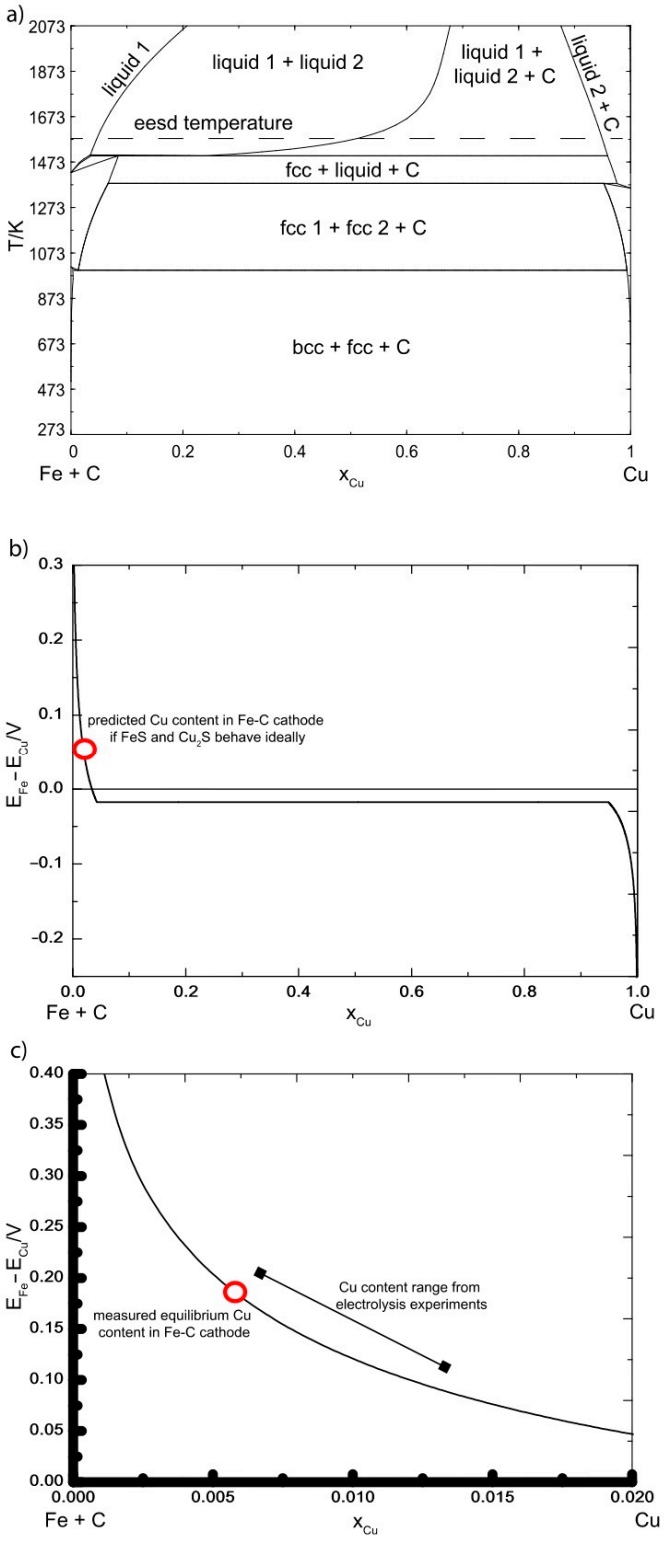

Figure 4. Phase diagram and electrochemical synthesis diagrams for the Fe—Cu—C system revealing potential for the selective deposition of iron and copper from chalcopyrite. (**a**) Fe—Cu—C phase diagram at carbon-saturation, x_C /(x_{Fe}+x_C) = 0.17 (4.2 wt%). (**b**) equilibrium electrochemical synthesis diagram for the (Fe—Cu—C)/(FeS—Cu_2S) system at 1300 °C. At this temperature, cast iron and copper phase separate to form two liquid solutions and solid carbon. (**c**) equilibrium electrochemical synthesis diagram for the (Fe—Cu—C)/(FeS—Cu_2S) system at 1300 °C for a cast iron cathode containing 4.8 wt% C (19 mol%) showing the measured copper content in the cast iron after equilibration as well as the cathode composition after electrolysis.

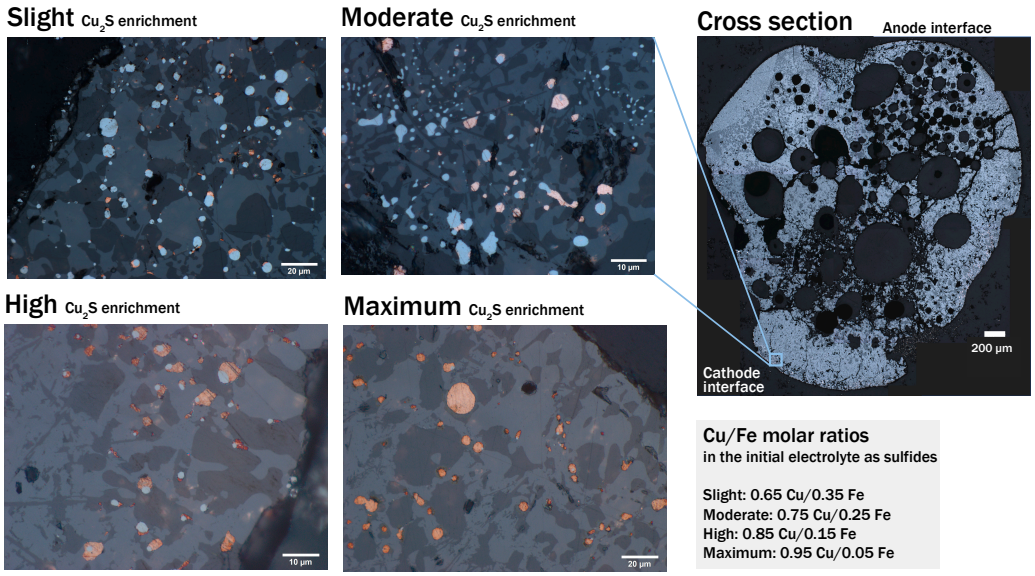

Figure 5. Micrographs of the dispersed metal at the graphite interface reveal that the electrolysis product evolves from being exclusively iron-rich for $CuFeS_2$ to majority copper-rich as the electrolyte composition is progressively enriched in Cu_2S. A cross-section of the moderate Cu_2S-enriched sample shows the extensive porosity observed after electrolysis. The Cu/Fe molar ratios in the initial electrolyte as sulfides for each sample (slight, moderate, high and maximum Cu_2S enrichment) can be seen in the bottom right corner.

Iron was the only product of electrolysis when decomposing $CuFeS_2$. Copper-rich phases were found when the initial Cu_2S content is slightly enriched, but iron remains the dominant product (EDS analysis of both phases in Tables S7–S9). The products of the moderately Cu_2S-enriched electrolyte show a fairly even mix of iron-rich and copper-rich precipitates (additional micrographs in Figure S30), while copper is the dominant product in the electrolytes with high and maximum Cu_2S enrichment. In these highly enriched electrolytes, iron-rich metal prills were still found, in contact with the copper-rich metal prills (SEM-EDS in Figure S31). The evolution of the electrolysis products can only be revealed by a dynamic study of electrolysis as it progresses, but the present results further indicate that iron forms preferentially at the cathode, owing to the lower decomposition potential and higher relative activity of FeS compared to Cu_2S. The deposited iron droplets are then in contact with the surrounding electrolyte and can enrich in copper, driven by thermodynamic mixing of the iron-copper metallic solution, or by depletion of the electrolyte. EDS analysis of the post-electrolysis sulfide phases in the cross-section reveals significant variation in the proportion of copper and iron across the electrolyte from the cathode to the anode (Figure S32). As iron precipitates preferentially, the concentration of iron in the adjacent electrolyte depletes. Copper-rich phases may precipitate once the local region is sufficiently iron depleted. As expected, as the bulk concentration of Cu_2S in the electrolyte increases, copper deposition is favored. However, the iron and copper phases present in Figure 5 may not reflect the products formed during electrolysis, as partitioning also occurs during cooling and solidification [40]. Copper and iron have a strong tendency towards immiscibility (accentuated by the presence of carbon, Figure 4a). Nevertheless, as the bulk concentration of Cu_2S in the electrolyte increases, the amount of metallic copper found at the cathode increases.

While the metal product could not be physically collected, the mass loss of the electrolyte provides an indication of anodic efficiency; only sulfur generated during electrolysis is expected to leave the electrolyte, with the corresponding production of metal. Accounting for mass losses due to thermal decomposition (via thermal control trials, described in Section 2.1.8), the average Faradaic efficiency for sulfur over 6 trials was 68%, with

high variability (Figure S33). The low volume of electrolyte and the small anode-cathode distance is insufficient to prevent back-reactions between sulfur and the metal droplets. Indeed, the high porosity of the electrolyte following electrolysis is evident in Figure 5, which adds variability and affects faradaic efficiency determined by this mass balance. Despite this variability, the electrolyzed samples consistently showed greater mass loss compared to the thermal trials, and increased sulfur deposition was observed on the quartz tube following electrolysis (Figures S34–S37). In situ observation also revealed regular bubbling only present with the application of the electrolytic current (Supplementary Video S1).

The electroactive ions in the electrolyte can be represented as S^{2-}, Fe^{2+}, and Cu^{+}. At high temperature with low pO_2, FeS is the sole iron sulfide stable, such that +II would be the dominant valency for iron in the electrolyte. This is significant as the multi-valency of iron has afflicted previous electrolytic systems dealing with iron. Efficiencies reported here are minimum estimates. The experiment is batch, so back-reactions between sulfur and the metal cathode are possible during cooling and full recovery of the produced metal is challenging at this scale. No evidence of side reactions has been observed, and the decomposition voltage of BaS and La_2S_3 are sufficiently high (Figure 2) so that they are true supporting electrolyte components.

At scale, iron will be extracted and periodically tapped as more liquid iron is produced, possibly as a Fe-C alloy in a first electrolysis stage. At that stage other metals more noble than iron such as Mo, Re or Ag can also be recovered [46], for example dissolved in the cast iron. The molten electrolyte, then depleted in iron (and other metals) can be subject to a subsequent electrolysis reaction which instead operates with a liquid copper cathode, also periodically tapped. The Cu-Fe-S ternary diagram (Figure S38) and our results suggest the transition from an iron-rich to a copper-rich product happens when the molar ratio in the electrolyte reaches about Cu/Fe=3 (compared to chalcopyrite in the feedstock which is typically Cu/Fe~1). The composition of the cathode as the electrolyte composition enriches in copper sulfide was investigated with experiments performed with cast iron or copper as liquid cathodes on a graphite stand. The set-up is similar to the 300 mA experiments (Figure S7) except that a graphite stand is holding the liquid metal cathode and electrolyte droplet, and serves as the cathode current collector. The composition of the liquid metal cathodes after electrolysis with each electrolyte sample as the enrichment of Cu_2S varies was evaluated with SEM-EDS, compiled in Figure 6. It should be noted that the measured bulk cathode composition may not reflect the electrolyzed metal in sum due to a partial dispersion of the metal product, especially in areas of contact between the graphite current collector and electrolyte (Figure S39). Nevertheless, as expected, as the initial Cu_2S content in the electrolyte increases, the concentration of copper in the iron cathode increases; and as the initial FeS content in the electrolyte decreases, the concentration of iron in the copper cathode decreases. Thermal control trials in absence of electrolysis were performed to evaluate the relative role of thermal mixing versus electrochemical mixing. The similar composition achieved for both the electrolysis and thermal trials shows the thermodynamic force of mixing between the cathode and electrolyte species is a strong determinant of the cathode composition.

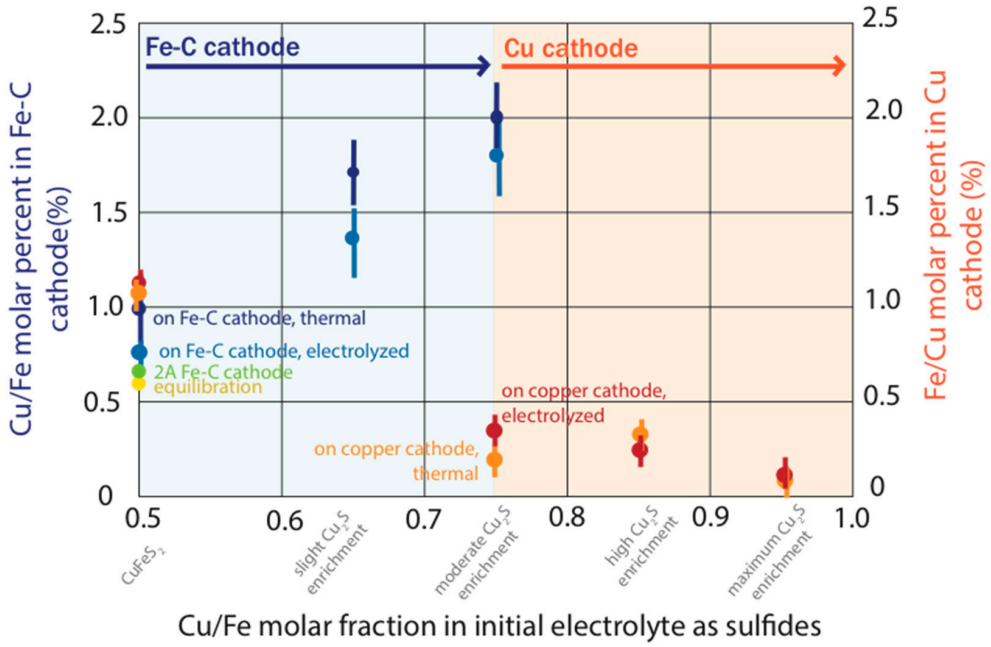

Figure 6. Measured composition of the metal cathodes after electrolysis and thermal treatments as the initial copper sulfide enrichment in the electrolyte increases. The iron extraction regime is on the left-hand side, with mol% Cu in cast iron on the vertical axis. The copper extraction regime is on the right-hand side, with mol% Fe in copper on the vertical axis. Compositions are measured by EDS and obtained from at least 5 readings: the average is plotted with the standard deviation range.

4. Discussion: Towards a Fully Electrified Step

The evidence presented above suggests that electrowinning of $CuFeS_2$ in the molten BaS-La_2S_3 electrolyte can selectively lead to liquid cast iron and copper thanks to their difference in chemical reactivity in the electrolyte and their quasi-immiscibility as metals. Experiments performed at the 50A scale (the scale-up process and results are described in [47]), allowed for collection and characterization of the metal product, revealing low iron concentration in the copper product (<2.5 wt%), and very low oxygen and sulfur (resp. 0.13 and 0.2 wt%). This outcome is remarkable, as such purity and composition of a liquid copper product at 1300°C suggest a product that may be directly treatable in a copper refining furnace. With the possibility of upstream impurity removal in the iron production stage, the electrorefining of copper altogether may not be necessary, depending on the actual sulfur content of the copper product. This copper product would then be obtained from two electrolytic decomposition reactions, written here with the solid compound stoichiometry for simplicity:

$$CuFeS_2 \rightarrow Fe(l) + S_2(g) + Cu_2S \quad (4)$$

$$Cu_2S \rightarrow Cu(l) + S_2(g) \quad (5)$$

The theoretical minimum cell voltage to drive reaction (4) at 1300 °C is 0.36 V (Figure 2), though actual electrolysis at the 7 A and 50 A scale [47] operated at a voltage of about 2 to 4 V, indicating auto-thermal or exothermic operation of the cell, similar to the practice in aluminum production. This extra heat can support melting of the initial feedstock. The conservative estimates of 60% faradaic efficiency coupled with the observed experimental voltage suggest an energy consumption per tonne of Fe of 3200–6400 kWh. Reaction (5) minimum decomposition voltage is 0.41 V, with actual measurement at 50 A scale of about 5 V (though this has not yet been optimized) [47]. With a cautious estimated faradaic efficiency at 50%, the energy consumption per tonne of Cu is estimated at 4220 kWh, which is comparable with the overall energy consumption in existing smelting [48].

Overall, there are no direct greenhouse gas or noxious emissions generated and indirect emissions may be eliminated with the use of renewable electricity. In comparison, the total global warming potential for copper from conventional pyrometallurgy is 1.1 to 8.9 kgCO_2/kg refined copper, with the large variation due to different local energy mixes, ore grades and reactors [49]. The co-production of CO_2-free cast iron (1.8 kg CO_2/kg Fe typical in the primary route), without any associated raw material costs, is a significant opportunity. The supporting electrolyte and sulfur may be re-circulated such that there are no consumable reactants. Excess sulfur generated by electrolysis can be condensed and safely stored, or possibly reprocessed to produce electricity. SO_2 emissions from the sulfidation step may be captured in a scrubber, or converted to sulfuric acid if economically justified.

Additional opportunities along the supply chain further enhance the potential of this approach.

4.1. A New Process Flowsheet

The electrolysis experiments show for the first time the feasibility of electrolytically decomposing chalcopyrite into its main elemental components–sulfur as anodic gas, and iron and copper as liquid cathode products–in the absence of oxygen. This supports a new process flowsheet, presented in Figure 7, in which liquid cast iron and liquid copper are sequentially produced and periodically recovered via tapping of the reactor, as found in other metallurgical processes. The periodic and partial tapping of the liquid cathode allows the current flow to be maintained and production to continue while recovering the metal. The absence of oxygen in the feed for electrolysis and in the electrolyte suggests a unique opportunity to manage the impurities in chalcopyrite thanks to pre-treatments upstream of electrolytic decomposition.

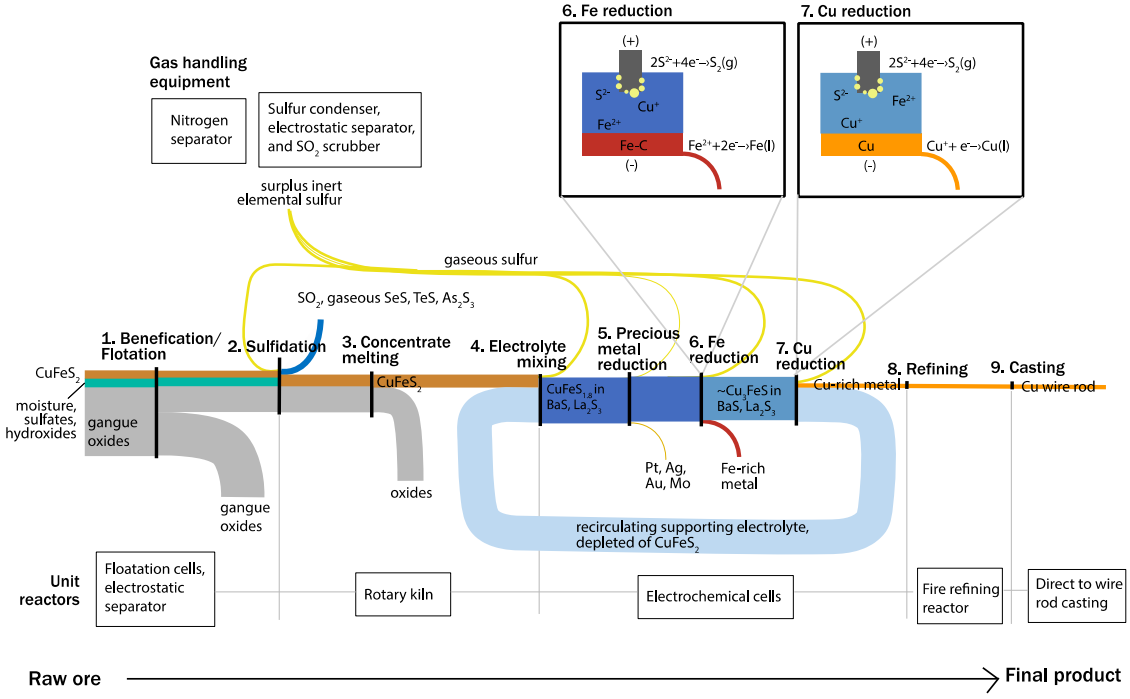

Figure 7. Schematic process flow for treating chalcopyrite, from raw ore to copper wire rod. Each vertical black line is a process step with the material inputs represented by horizontal flows on the left-hand side, and process outputs on the right. The unit reactors for each process step are shown in the boxes below, with the gas handling equipment required shown above the diagram. Schematics of the iron and copper reduction cells and the half-cell reactions are shown above. The width of flows drawn are relative, not to scale.

4.2. Sulfidation

Chalcopyrite ores are typically a physical mix of sulfide/sulfates and oxide (gangue) phases, with some moisture. Moisture is readily removed today around 180 °C, with limited energy consumption and the possibility using renewable energy [50]. To process in the sulfide regime, i.e., in absence of oxygen-containing species, the oxide, sulfate, and hydrated compounds must be converted to sulfides. Elimination of oxygen from the concentrate feedstock prior to mixing with the supporting electrolyte is necessary to avoid oxysulfide formation and degradation of the electrolyte [51]. Sulfidation of these copper compounds is exothermic, indicating that the reaction may be conducted with little to no external heating. Depending on the oxide content of the feed (and therefore heat generation), sulfidation may provide a means to preheat and melt feedstocks prior to electrolysis [52].

A sulfidation treatment, described in Section 2.1.2, was effective to yield a feed consisting primarily of $CuFeS_2$. As shown in the process flow sheet, the sulfur produced during electrolytic decomposition may be recycled to this step for this purpose. The sulfidation pre-treatment is promising for upstream impurity handling [34]. Chalcopyrite contains a multitude of impurities, which are present in variable forms and concentrations. While impurities are reportedly lacking from North American ores, they are of wide interest and in urgent need of improved processing in South America, especially the hazardous Group 15 elements. Stinn et al. [52] demonstrate the applicability of sulfidation to decrease arsenic, antimony and selenium in enargite-rich and tennantite ore by 72–99%, with low costs and environmental impacts. Determining the conditions to treat a complex feedstock requires careful thermodynamic and mineralogical analysis of the initial phase, morphology and concentration of the impurities present, in addition to experimental testing. Nevertheless, pS_2/pSO_2 may be a flexible and effective process lever for a range of mineralogies. A similar concept utilizing sulfur injections to extract nickel from nickeliferous laterite ore is practiced industrially by PT Inco [53]. Handling sulfur-rich gas streams is well-established in the metallurgical, and oil and gas industries. The presence of sulfates may lead to corrosion of metal pipes, so the transformation of any sulfates in the feedstock to sulfides and SO_2(g) as a pre-treatment will also mitigate corrosion.

4.3. Oxide Phase Separation

Floatation is used today as one of the mineral processes to effectively separate oxide and sulfide phases from copper ores, and here may be performed before or after sulfidation treatments, depending on the mineralogy and targeted recovery of impurities. Before electrolysis, any remaining oxide phases must be removed. This may be accomplished simply by the immiscibility that occurs upon melting. Most sulfide (chalcopyrite, pyrite, chalcocite) and oxide (silicates, aluminates) phases from copper sulfide ores are immiscible at low partial pressure of oxygen, so phase separation occurs upon melting of the sulfide phase around 1000 °C. This was confirmed to be experimentally reproducible, as described in Section 2.1.3. To improve process efficiency, this oxide removal step may be performed during any sulfidation treatments. Due to the exothermic nature of concentrate sulfidation, excess energy may be used to melt the concentrate, depending on the copper and iron oxide content of the feed sulfidation.

In conventional smelting, a precise heat balance must be maintained by preparation of the concentrate. In this alternative process flow, the heat generated during sulfidation of residual copper oxides may be balanced to melt excess gangue material, enabling the recovery of copper from lower grade and finer-grained feedstocks than would be conventionally upgraded with physical separation. This could simultaneously reduce the burden of floatation, or allow the substitution of floatation with a simple electrostatic separation step. This approach would have the additional benefit of recovering the gangue in a condensed, inert form in contrast to massive tailing dams.

4.4. Deposition of Electro-Negative and electro-positive elements

Electrolytic decomposition in molten sulfides also presents an opportunity to remove electro-positive and electro-negative species present in the electrolyte. This concept was demonstrated by Sahu et al. [46] with the selective reduction in copper, molybdenum and rhenium sulfides from a molten sulfide electrolyte. Rhenium sulfide spontaneously decomposes at 1225 °C, while the selective decomposition of MoS_2 with respect to Cu_2S was demonstrated. Therefore, elements such as Mo, Re (and other highly electronegative elements present in chalcopyrite such as the PGM's, Ag, Au, and Bi) will be the first to collect at the cathode. The current requirements for this deposition are low relative to iron and copper (and in fact no current is required to decompose ReS_2 and Bi_2S_3), as shown in Figure 2. The first cathode should therefore collect these precious metals. Iron shows solubility with these elements, or a solid cathode placed physically above the iron cathode (at a lower potential with respect to the anode) may be employed to collect the impurities. All chalcopyrite impurities are expected to either be removed by sulfidation and pre-melting or deposit before the copper electrowinning step, as Cu_2S is the most electropositive compound. At the anode, any remaining anions: selenides, tellurides and arsenides will decompose at a lower potential than FeS and Cu_2S. Collecting impurities as metals on a cathode, or as gaseous species in the anodic gas, with the sole use of electricity, is transformative compared to conventional smelting and aqueous electrorefining, where several pyrometallurgical or hydrometallurgical steps are necessary prior to accessing sufficiently concentrated streams for further precipitation or reduction in the corresponding metals or compounds. Further investigation of this approach is needed, and is proposed as future work in scaled-up reactors [47].

4.5. Refining and Casting

While the sequential deposition of iron and copper provide iron-rich and copper-rich phases, further treatment for a marketable product would be required. The cast iron may be marketable, but the removal of residual copper would allow greater applicability. Here, there is an opportunity to form a synergy with the growing volumes of end-of-life contaminated steel scrap to treat both streams and invest in copper removal technologies [54]. The copper-rich product that contains <0.2% S, <0.1 wt%O and up to 3 wt% Fe [47] is similar to copper scrap that can be refined in holding and fire refining furnaces to 99.9% copper to achieve a 'high conductivity, fire refined' grade with wide applicability [55]. State-of-the-art holding and casting furnaces can control the final sulfur and oxygen concentration and cast wire rods directly, in the same facility as ore handling and extraction.

4.6. Economic Feasibility

Due to the high current density and low cell voltage demonstrated in this work, molten sulfide electrolysis for commodity copper production fits within the process space for economic feasibility. While a full economic evaluation is outside the scope of this paper, the conversion costs of copper in the incumbent smelting-converting-electrorefining route can be used as a benchmark to derive key engineering metrics a new process based on direct electrochemical decomposition must achieve. This method and the corresponding targets are found in a prior work by Allanore [48]. For the conversion costs of an electrolytic process for copper extraction to be on par with the incumbent processes, electricity consumption use must be around 3900 kWh/t. Energy consumption of 4220 kWh/t was measured in this work, with a cell voltage of 5 V and 50% Faradaic efficiency based on metal recovery. Increasing Faradaic efficiency modestly to 60% would bring energy consumption to the target, and is expected with tapping of the metal product and controlled anode-cathode spacing to avoid back-reactions. To compete in terms of productivity (tonnes/day), a cathodic current density of at least 0.23 A/cm^2 is required, which the demonstrated current density of 1.5 A/cm^2 exceeds. This high current density allows for a highly efficient footprint, such that a total cathodic area of molten sulfide electrolysis cell of only ~1250 m^2 would provide 400 ktpa copper. Such a footprint may support mineral processing closer to

copper mine sites, which often coincide with areas of affordable, abundant solar energy. This process may also offer an economically viable pathway for iron production. If the cell voltage can be controlled to 2–3 V, the target of 3900 kWh/t provided by Allanore for a hypothetical iron extraction may also be met. The capital costs of a molten sulfide electrolysis facility may be explored with the work by Stinn and Allanore [56], which demonstrates that high-temperature, high current density reactors tend to minimize cell capital cost. The opportunities along the supply chain described above, to flexibly process unconventional ore grades and fines, reduce the burden of flotation by using oxide melting, efficiently recover impurities upstream by sulfidation and selective electrodeposition, and direct cast to final products offer avenues outside of the conventional paradigm for further economic advantage.

The availability and cost of the supporting electrolyte components investigated herein, BaS and La_2S_3, is an important consideration for larger scale implementation. These compounds can be produced from $BaSO_4$ (mineral barite, global production of 7 Mt/year in 2021 [56]) and La_2O_3 (~23 wt% of mineral bastnaesite, global production of ~280 kt/year in 2021 [57]). The process involves sulfidation [34], already demonstrated at a kg-scale for these compounds [46] and at the more than 100 kt/year for other minerals. Ba and La both score relatively low across the three main criticality dimensions: supply risk, environmental implications and vulnerability to supply restriction [58,59]. Due to the high decomposition potential and thermal stability of both components, and with proper pre-treatments to eliminate oxygen from the concentrate feedstock, the supporting electrolyte will not appreciably degrade during electrolysis. However, some oxygen contamination and entrainment to the liquid metal during casting is possible, and is better studied at the pilot scale. Trace oxygen is manageable, though may lead to carbothermic reduction in iron or copper in the presence of the carbon anode, reactions that shall be minimized to avoid direct CO/CO_2(g) emissions.

5. Conclusions

The electrolytic system investigated here shows promise for divorcing liquid copper production from oxygen to drastically simplify the supply chain and the handling of ancillary impurities. The BaS-La_2S_3 electrolyte was demonstrated to support high solubility for the feedstock with remarkably high current densities (1.5 A/cm^2), to exceed the productivity standards in industrial metal production [48]. Liquid metal is ideal for further processing and casting, and may be continuously tapped from the electrolyzers. The operating temperature of 1200–1400 °C is compatible with established refractories and heat management techniques. The graphite anode is readily available and inert.

Due to the unique interactions between iron and copper, perhaps further accentuated by the supporting electrolyte, the deposition of iron and copper may be performed sequentially. For the first time, a complex ore may be effectively separated into its elemental components. The multi-valency of iron is a hindrance in most electrolytic techniques involving iron, but the Fe^{2+} ion is stable in this sulfide regime.

Copper minerals are typically found in regions with abundant solar energy, but scarce water supply. This processing route, with a highly efficient footprint, may be compatible with operation on remote mine-sites. Several unique processing possibilities may offer flexible processing of variable copper minerals: the sulfidation of impurities, the deposition of electro-positive and electro-negative elements and the avoidance of aqueous refining for the direct casting of wire-rod. Flexible, local production may enhance the domestic supply of critical metals. With renewable energy, this processing route decouples metal production from greenhouse gas emissions. Molten sulfide electrolysis may be viable for other sulfide minerals, or even oxide feedstocks for a new paradigm of high-throughput, sustainable metal production.

Supplementary Materials: The following supporting information can be downloaded at: https://www.mdpi.com/article/10.3390/met12091440/s1, Figure S1: Phase identification for the initial chalcopyrite concentrate; Figure S2: Phase identification for chalcopyrite concentrate after sulfidation; Figure S3: The sulfidized chalcopyrite concentrate after melting to remove residual oxide phases; Figure S4: Oxide slag phase separated on top of the sulfide matte after induction melting in excess of 1100 °C; Figure S5: SEM image of the synthesized electrolyte for the 300 mA chalcopyrite-containing experiments, with the rectangle showing the area of the EDS scan; Figure S6: Elemental peaks from EDS scan of region in Figure S5; Figure S7: Image of graphite stand cathode and molten electrolyte droplet with the anode suspended from above in the thermal-imaging floating zone furnace; Figure S8: Voltage trace for the electrolysis of the 'natural-1′ trial; Figure S9: Voltage trace for the electrolysis of the 'natural-2′ trial; Figure S10: Voltage trace for the electrolysis of the 'slight-1′ trial; Figure S11: Voltage trace for the electrolysis of the 'slight-2′ trial; Figure S12: Voltage trace for the electrolysis of the 'moderate-1′ trial; Figure S13: Voltage trace for the electrolysis of the 'moderate-2′ trial; Figure S14: Voltage trace for the electrolysis of the 'high-1′ trial; Figure S15: Voltage trace for the electrolysis of the 'high-2′ trial; Figure S16: Voltage trace for the electrolysis of the 'maximum-1′ trial; Figure S17: Cross-section of the thermal trial of natural chalcopyrite electrolyte on graphite; Figure S18: Cross section of the natural-graphite thermal trial at higher power with vacuum (−10 *psig*) applied; Figure S19: Voltage trace for the electrolysis of the 'natural-Fe' trial; Figure S20: Voltage trace for the electrolysis of the 'slight-Fe' trial; Figure S21: Voltage trace for the electrolysis of the 'moderate-Fe' trial; Figure S22: Voltage trace for the electrolysis of the 'moderate-Cu' trial; Figure S23: Voltage trace for the electrolysis of the 'high-Cu' trial; Figure S24: Voltage trace for the electrolysis of the 'maximum-Cu' trial; Figure S25: Schematic of the 7A electrolysis cell; Figure S26: Applied current and measured cell voltage for the 7A iron deposition experiment; Figure S27: Additional micrographs of metallic iron product in chalcopyrite-containing electrolyte electrolyzed on graphite; Figure S28: Current and measured outlet gas composition (CO, H_2S) for 7A iron deposition experiment; Figure S29: Sulfur deposit on furnace cap (left) and SEM-EDS imaging of the deposit (right) from the 7A iron deposition experiment; Figure S30: Cross section of 'moderate-1′ droplet after electrolysis; Figure S31: SEM-EDS mapping of electrolysis products from the slightly enriched copper sulfide electrolyte; Figure S32: Atomic Fe/Cu ratio in the electrolyte at various points of the cross-section of the 'High-Cu cathode' sample; Figure S33: Faradaic efficiency calculated from mass loss after electrolysis for 300 mA experiments on graphite; Figure S34: Images of the quartz tube in the thermal imaging furnace after electrolysis and after only heating; Figure S35: SEM images of sulfur particles collected from the quartz tube; Figure S36: EDS mapping of the sulfur particles in Figure S35; Figure S37: EDS spectrum and concentration of detected elements from spot indicated in Figure S36; Figure S38: Cu-Fe-S ternary phase diagram; Figure S39: Cross section of 'slight-Fe' electrolyte and cast iron cathode after electrolysis; Table S1: Quantitative elemental analysis of EDS scan of synthesized electrolyte for the chalcopyrite-containing 300 mA experiments; Table S2: Experimental notes from electrolyzing chalcopyrite-containing and Cu_2S-enriched electrolyte on graphite at the 300 mA scale title; Table S3: Experimental notes from electrolyzing electrolyte samples on copper and cast iron cathodes at the 300 mA scale; Table S4: Composition of the initial cast iron cathode for the 7A iron deposition experiment; Table S5: Change in composition of the cathode pre- and post-electrolysis for the 7A iron deposition experiment; Table S6: Composition of the cathode pre- and post-electrolysis for the 7A iron deposition experiment; Table S7: Average composition of the iron-rich electrolysis product in the slightly enriched copper sulfide electrolyte; Table S8: Average composition of the iron-rich electrolysis product in contact with the copper-rich phase in the slightly enriched copper sulfide electrolyte; Table S9: Average composition of the copper-rich electrolysis product in contact with the iron-rich phase in the slightly enriched copper sulfide electrolyte; Table S10: Measured wt% of iron and copper in the electrolyte at various points of the cross-section of the 'High-Cu cathode' sample; Video S1: Video of the 'High-1′ 300 mA trial in the thermal imaging furnace.

Author Contributions: Conceptualization: A.A., B.C., K.E.D., M.E.W., C.S. and L.R., Methodology: K.E.D.: C.S., L.R., E.B.-K., M.E.W., C.B. and C.G., Supervision: A.A., Writing—original draft: K.E.D., Writing—reviewing and editing: A.A., K.E.D., E.B.-K., C.S., M.E.W. and B.C. All authors have read and agreed to the published version of the manuscript.

Funding: This project was funded by the U.S. Department of Energy's Office of Energy Efficiency and Renewable Energy (EERE) under the Advanced Manufacturing Office (AMO) Emerging Research Exploration Award Number DE-EE0008316.

Institutional Review Board Statement: Not applicable.

Informed Consent Statement: Not applicable.

Data Availability Statement: Not applicable.

Acknowledgments: R. Yagi and A. Caldwell established rigorous experimental protocols in the lab and provided extremely helpful expertise and insights. Freeport McMoRan graciously provided concentrate samples.

Conflicts of Interest: The authors declare no conflict of interest.

References

1. Frame, L. Reconstructing Ancient Technologies: Chalcolithic Crucible Smelting at Tal-i Iblis, Iran. In *Scientific Research on Ancient Asian Metallurgy: Proceedings of the Fifth Forbes Symposium at the Freer Gallery of Art*; Archetype Books: London, UK, 2012; pp. 183–204.
2. Schlesinger, M.E.; King, M.J.; Sole, K.C.; Davenport, W.G. *Extractive Metallurgy of Copper*, 5th ed.; Elsevier: Oxford, UK, 2011, ISBN 9788578110796.
3. Kojo, I.V.; Jokilaakso, A.; Hanniala, P. Flash Smelting and Converting Furnaces: A 50 Year Retrospect. *JOM* **2000**, *52*, 57–61. [CrossRef]
4. Matos, G.R.; Miller, L.D.; Barry, J.J. *Historical Global Statistics for Mineral and Material Commodities*; Copper: Reston, VA, USA, 2015.
5. Elshkaki, A.; Graedel, T.E.; Ciacci, L.; Reck, B. Copper Demand, Supply, and Associated Energy Use to 2050. *Glob. Environ. Chang.* **2016**, *39*, 305–315. [CrossRef]
6. Attwood, J. *The World Will Need 10 Million Tons More Copper to Meet Demand*; Bloomberg: New York, NY, USA, 2022.
7. Valenta, R.K.; Kemp, D.; Owen, J.R.; Corder, G.D.; Lèbre, E. Re-Thinking Complex Orebodies: Consequences for the Future World Supply of Copper. *J. Clean. Prod.* **2019**, *220*, 816–826. [CrossRef]
8. Northey, S.; Mohr, S.; Mudd, G.M.; Weng, Z.; Giurco, D. Modelling Future Copper Ore Grade Decline Based on a Detailed Assessment of Copper Resources and Mining. *Resour. Conserv. Recycl.* **2014**, *83*, 190–201. [CrossRef]
9. Lezak, S.; Cannon, C.; Blank, T.K. *Low-Carbon Metals for a Low-Carbon World: A New Energy Paradigm for Mines*; Rocky Mountain Institute: Boulder, CO, USA, 2019.
10. Redniss, L. *Oak Flat: A Fight for Sacred Land in the American West*; Random House: New York, NY, USA, 2020.
11. Xu, B.; Ma, Y.; Gao, W.; Yang, J.; Yang, Y.; Li, Q.; Jiang, T. A Review of the Comprehensive Recovery of Valuable Elements from Copper Smelting Open-Circuit Dust and Arsenic Treatment. *JOM* **2020**, *72*, 3860–3875. [CrossRef]
12. Safarzadeh, M.S.; Moats, M.S.; Miller, J.D. Recent Trends in the Processing of Enargite Concentrates. *Miner. Process. Extr. Metall. Rev.* **2014**, *35*, 283–367. [CrossRef]
13. Davidson, V. Copper Market Outlook: Transitioning to Deficits. In Proceedings of the Copper to World Conference, Santiago, Chile, 3–5 April 2017.
14. Fu, X.; Olivetti, E.A. High-Resolution Insight into Materials Criticality: Quantifying Risk for By- Product Metals from Primary Production: Quantifying Risk for By-Product High-Resolution Insight into Materials Criticality: Quantifying Risk for Byproduct Metals from Primary. *J. Ind. Ecol.* **2018**, *23*, 452–465. [CrossRef]
15. Schlesinger, M.E.; King, M.J.; Sole, K.C.; Davenport, W.G. Electrolytic Refining. In *Extractive Metallurgy of Copper*, 5th ed.; Elsevier: Oxford, UK, 2011; ISBN 9788578110796. pp. 251–280.
16. Kavlak, G.; Graedel, T.E. Global Anthropogenic Selenium Cycles for 1940–2010. *Resour. Conserv. Recycl.* **2013**, *73*, 17–22. [CrossRef]
17. Kavlak, G.; Graedel, T.E. Global Anthropogenic Tellurium Cycles for 1940–2010. *Resour. Conserv. Recycl.* **2013**, *76*, 21–26. [CrossRef]
18. Moats, M.; Alagha, L.; Awuah-Offei, K. Towards Resilient and Sustainable Supply of Critical Elements from the Copper Supply Chain: A Review. *J. Clean. Prod.* **2021**, *307*, 127207. [CrossRef]
19. Francescone, K. Tracing Indium Production to the Mines of the Cerro Rico de Potosí. *Econ. Anthropol.* **2018**, *6*, 110–122. [CrossRef]
20. International Energy Agency (IEA). *The Role of Critical Minerals in Clean Energy Transitions*; IEA: Paris, France, 2021.
21. Granata, G.; Miura, A.; Liu, W.; Pagnanelli, F.; Tokoro, C. Iodide-Assisted Leaching of Chalcopyrite in Acidic Ferric Sulfate Media. *Hydrometallurgy* **2019**, *186*, 244–251. [CrossRef]
22. Habashi, F. Abandoned but Not Forgotten—The Recent History of Copper Hydrometallurgy. *Metall* **2006**, *60*, 459–465.
23. Peters, E. Direct Leaching of Sulfides: Chemistry and Applications. *Met. Trans. B* **1976**, *7*, 505–517. [CrossRef]
24. Habashi, F.; Yostos, B.I. Copper From Chalcopyrite By Direct Reduction. *J. Met.* **1977**, *29*, 11–16. [CrossRef]
25. Murthy, G.G.K.; Elliott, J.F. Smelting of Iron-Oxy-Sulfide Melts Using Solid Carbon. *ISIJ Int.* **1994**, *34*, 548–554. [CrossRef]
26. Coursol, P.; Mackey, P.J. Energy Consumption in Copper Sulphide Smelting. *Mater. Sci.* **2010**, *2*, 649–668.

27. Moreno-Leiva, S.; Haas, J.; Junne, T.; Valencia, F.; Godin, H.; Kracht, W.; Nowak, W.; Eltrop, L. Renewable Energy in Copper Production: A Review on Systems Design and Methodological Approaches. *J. Clean. Prod.* **2020**, *246*, 118978. [CrossRef]
28. Townsend, C. *Process for the Reduction of Ores*; United States Pattent Office: Brooklyn, NY, USA, 1906.
29. Ge, X.L.; Seetharaman, S. The Salt Extraction Process—A Novel Route for Metal Extraction Part 2—Cu/Fe Extraction from Copper Oxide and Sulphides. *Miner. Process. Extr. Metall.* **2012**, *119*, 93–100. [CrossRef]
30. Tan, M.; He, R.; Yuan, Y.; Wang, Z.; Jin, X. Electrochemical Sulfur Removal from Chalcopyrite in Molten NaCl-KCl. *Electrochim. Acta* **2016**, *213*, 148–154. [CrossRef]
31. Kartal, L.; Timur, S. Direct Electrochemical Reduction of Copper Sulfide in Molten Borax. *Int. J. Miner. Metall. Mater.* **2019**, *26*, 992–998. [CrossRef]
32. Sokhanvaran, S.; Lee, S.; Lambotte, G.; Allanore, A. Electrochemistry of Molten Sulfides: Copper Extraction from BaS-Cu_2S. *J. Electrochem. Soc.* **2016**, *163*, 115–120. [CrossRef]
33. Daehn, K.; Allanore, A. Electrolytic Production of Copper from Chalcopyrite. *Curr. Opin. Electrochem.* **2020**, *22*, 110–119. [CrossRef]
34. Stinn, C.; Allanore, A. Selective Sulfidation of Metal Compounds. *Nature* **2021**, *602*, 78–83. [CrossRef]
35. Stinn, C.; Nose, K.; Okabe, T.; Allanore, A. Experimentally Determined Phase Diagram for the Barium Sulfide-Copper (I) Sulfide System Above 873 K (600 °C). *Metall. Mater. Trans. B* **2017**, *48*, 2922–2929. [CrossRef]
36. Boury, C.; Allanore, A. Liquid State Properties and Solidification Features of the Pseudo Binary BaS-La_2S_3. *Sci. Rep.* **2021**, *11*, 18189. [CrossRef]
37. Allanore, A. Features and Challenges of Molten Oxide Electrolytes for Metal Extraction. *J. Electrochem. Soc.* **2014**, *162*, E13–E22. [CrossRef]
38. Winkel, L.; Wochele, J.; Ludwig, C.; Alxneit, I.; Sturzenegger, M. Decomposition of Copper Concentrates at High-Temperatures: An Efficient Method to Remove Volatile Impurities. *Miner. Eng.* **2008**, *21*, 731–742. [CrossRef]
39. Nakanishi, B.R.; Allanore, A. Electrochemical Study of a Pendant Molten Alumina Droplet and Its Application for Thermodynamic Property Measurements of Al-Ir. *J. Electrochem. Soc.* **2017**, *164*, E460–E471. [CrossRef]
40. Nakagawa, Y. Liquid Immiscibility in Copper-Iron and Copper-Cobalt Systems in the Supercooled State. *Acta Metall.* **1958**, *6*, 704–711. [CrossRef]
41. Eichis, B.A.; Sokolova, T.G.; Velikanov, A.A. Influence of Additions of Na_2S on the Electrochemical Properties of Liquid Silver Sulfide. *Sov. Electrochem.* **1971**, *7*, 1447–1449.
42. Vivian, R.E. The Electrolysis of Molten Antimony Sulfide. *Trans. Electrochem. Soc.* **1936**, *69*, 4. [CrossRef]
43. Kaptay, G. The Conversion of Phase Diagrams of Solid Solution Type into Electrochemical Synthesis Diagrams for Binary Metallic Systems on Inert Cathodes. *Electrochim. Acta* **2012**, *60*, 401–409. [CrossRef]
44. Wagner, M.-E.; Allanore, A. Non-Standard State Thermodynamics of Metal Electrodeposition. *Electrochim. Acta* **2021**, *389*, 138442. [CrossRef]
45. Wang, C.; Nagasaka, T.; Hino, M.; Ban-Ya, S. Copper Distribution between FeS-Alkaline or -Alkaline Earth Metal Sulfide Fluxes and Carbon Saturated Iron Melt. *ISIJ Int.* **1991**, *31*, 1309–1315. [CrossRef]
46. Sahu, S.K.; Chmielowiec, B.; Allanore, A.; Member, I.S.E. Electrochimica Acta Electrolytic Extraction of Copper, Molybdenum and Rhenium from Molten Sul Fi de Electrolyte. *Electrochim. Acta* **2017**, *243*, 382–389. [CrossRef]
47. Daehn, K.E.; Benderly-Kremen, E.; YAGI, R.; Stinn, C.; Boury, C.; Rush, L.T.; Wagner, M.-E.; Allanore, A. Scaling up Molten Sulfide Electrolysis for Liquid Copper Production from Chalcopyrite. In Proceedings of the Copper 2022 Conference, Santiago, Chile, 13–17 November 2022.
48. Allanore, A. Electrochemical Engineering for Commodity Metals Extraction. *Electrochem. Soc. Interface* **2017**, *26*, 63–68. [CrossRef]
49. Dong, D.; van Oers, L.; Tukker, A.; van der Voet, E. Assessing the Future Environmental Impacts of Copper Production in China: Implications of the Energy Transition. *J. Clean. Prod.* **2020**, *274*, 122825. [CrossRef]
50. Behar, O.; Peña, R.; Kouro, S.; Kracht, W.; Fuentealba, E.; Moran, L.; Sbarbaro, D. The Use of Solar Energy in the Copper Mining Processes: A Comprehensive Review. *Clean. Eng. Technol.* **2021**, *4*, 100259. [CrossRef]
51. Stinn, C.; Allanore, A. Selective Sulfidation for Rare Earth Element Separation. In *Rare Metal Technology 2022*; Ouchi, T., Ed.; The Minerals, Metals & Materials Society: Cham, Switzerland, 2022; pp. 259–278.
52. Stinn, C.; Gutierrez, C.; Daehn, K.E.; Allanore, A. Sulfidation for Copper Mineral Processing and Impurity Management. In Proceedings of the Copper 2022 Conference, Santiago, Chile, 13–17 November 2022.
53. Morcali, M.; Khajavi, L.T.; Dreisinger, D.B. Extraction of Nickel and Cobalt from Nickeliferous Limonitic Laterite Ore Using Borax Containing Slags. *Int. J. Miner. Process.* **2017**, *167*, 27–34. [CrossRef]
54. Daehn, K.E.; Serrenho, A.C.; Allwood, J. Finding the Most Efficient Way to Remove Residual Copper from Steel Scrap. *Metall. Mater. Trans. B* **2019**, *50*, 1225–1240. [CrossRef]
55. Hormesa. Conticast Copper Scrap Fire Refining Process. Available online: https://hormesa-group.com/wp-content/uploads/2018/09/Catalogo-piro-refinacion----Fire-refining-catalog.pdf (accessed on 25 August 2022).
56. Stinn, C.; Allanore, A. Estimating the Capital Costs of Electrowinning Processes. *Electrochem. Soc. Interface* **2020**, *29*, 44–49. [CrossRef]
57. McRae, M. *Barite*; Minerals Commodity Summaries; U.S. Geological Survey: Reston, VA, USA, 2022.

58. Cordier, D. *Rare Earths*; Minerals Commodity Summaries; U.S. Geological Survey: Reston, VA, USA, 2022.
59. Graedel, T.E.; Harper, E.M.; Nassar, N.T.; Nuss, P.; Reck, B.K.; Turner, B.L. Criticality of Metals and Metalloids. *Proc. Natl. Acad. Sci. USA* **2015**, *112*, 4257–4262. [CrossRef] [PubMed]